Magnetization dynamics driven by displacement currents across a magnetic tunnel junction

C.K. Safeer[1,*] Paul S. Keatley,[2] Witold Skowroński,[3] Jakub Mojsiejuk,[3] Kay Yakushiji,[4]
Akio Fukushima,[4] Shinji Yuasa,[4] Daniel Bedau,[5] Fèlix Casanova,[6,7] Luis E. Hueso,[6,7]
Robert J. Hicken,[2] Daniele Pinna,[1] Gerrit van der Laan,[8] and Thorsten Hesjedal[1,†]

[1] *Clarendon Laboratory, Department of Physics, University of Oxford, Oxford, OX1 3PU, United Kingdom*
[2] *Department of Physics and Astronomy, University of Exeter, Stocker Road, Exeter, EX4 4QL, United Kingdom*
[3] *Institute of Electronics, AGH University of Kraków, Al. Mickiewicza 30, 30-059 Kraków, Poland*
[4] *National Institute of Advanced Industrial Science and Technology, Research Center for Emerging Computing Technologies, Tsukuba, Ibaraki 305-8568, Japan*
[5] *Western Digital, San Jose Research Center, 5601 Great Oaks Parkway San Jose, CA 95119, United States*
[6] *CIC nanoGUNE BRTA, 20018 Donostia-San Sebastián, Basque Country, Spain*
[7] *IKERBASQUE, Basque Foundation for Science, 48009 Bilbao, Basque Country, Spain*
[8] *Science Division, Diamond Light Source, Harwell Science and Innovation Campus, Didcot, Oxfordshire OX11 0DE, United Kingdom*

Understanding the high-frequency transport characteristics of magnetic tunnel junctions (MTJs) is crucial for the development of fast-operating spintronics memories and radio frequency devices. Here, we present the study of a frequency-dependent capacitive current effect in CoFeB/MgO-based MTJs and its influence on magnetization dynamics using a time-resolved magneto-optical Kerr effect technique. In our device, operating at gigahertz frequencies, we find a large displacement current of the order of mA, which does not break the tunnel barrier of the MTJ. Importantly, this current generates an Oersted field and spin-orbit torque, inducing magnetization dynamics. Our discovery holds promise for building robust MTJ devices operating under high current conditions, also highlighting the significance of capacitive impedance in high-frequency magnetotransport techniques.

I. INTRODUCTION

Magnetic tunnel junctions (MTJs) serve as fundamental components in various spintronics devices, mainly relying on the tunneling magnetoresistance (TMR) effect [1–4]. In TMR devices, the electrical resistance depends on the relative alignment of the moments in the magnetic layers, facilitating efficient data read-out in memory devices such as hard disk drives [5] and magnetic random-access memory (MRAM) [6]. Moreover, the spin torque effects generated by current [7] or voltage [8] in MTJs can be used to electrically switch the magnetization. The speed of both

the reading and writing processes plays a pivotal role in the development of fast-operating memories, as needed in modern devices operating at gigahertz (GHz) frequencies.

In addition to data storage and memory applications, MTJs are also building blocks for dynamic radio frequency (rf) spintronic components. Primarily, these include spin torque nano-oscillators [9–11] that exhibit autonomous precession of the magnetization by leveraging antidamping spin-transfer torques, energy harvesters [12], rf detectors [13,14], and magnonic devices that utilize the propagation and manipulation of spin waves in ferromagnetic materials [15]. Regarding MTJ nano-oscillators, their capacity to detect and manipulate rf signals at the nanoscale holds promise for applications in rf signal processing, wireless communication [16], and emerging neuromorphic technologies [17]. Magnonic devices are envisioned to be pivotal for the development of low-power electronics in the future [15]. In addition to these practical applications, experimental rf magnetotransport techniques, such as spin torque ferromagnetic resonance (ST-FMR) [18,19], have

---

*Contact author: safeer.chenattukuzhiyil@physics.ox.ac.uk
†Contact author: thorsten.hesjedal@physics.ox.ac.uk

been extensively employed to gain insight into fundamental spintronics principles, particularly current-induced magnetization dynamics in various systems. All these factors underscore the practical and fundamental significance of studying frequency-dependent physical effects in MTJs.

A well-known frequency-dependent effect observed in MTJs is the magnetocapacitance effect [20,21], where MTJs can behave like leaky capacitors. Analogous to TMR, they exhibit the tunnel magnetocapacitance (TMC) effect [20,22], where the overall capacitance depends on the relative alignment of the magnetization (parallel or antiparallel) of the free and fixed magnetic layers within the MTJ. The strength of the TMC is strongly dependent on frequency [22] and has even been reported to reverse sign within a specific frequency range [23,24]. Importantly, the capacitive reactance of MTJs varies with frequency, with low reactance expected at high frequencies [20,22–24] that leads to significant displacement currents. The latter is not an actual charge flow across a capacitor; instead, it was introduced according to the Ampère-Maxwell equation to explain the magnetic fields resulting from changing electric fields in a dielectric medium, such as the MgO tunnel barrier in our MTJ device. The large displacement current in MTJ circuits at high frequencies can be harnessed to induce magnetization dynamics. To the best of our knowledge, this observation has not been reported previously.

In this article, using specially designed CoFeB/MgO/CoFeB-based MTJ devices, we report an unprecedented study of the magnetization dynamics induced by displacement currents across an MTJ. Our findings reveal that substantial displacement currents, in the range of mA, flow through the MTJ circuit at GHz frequencies. Remarkably, this substantial current does not damage the MTJs, as the displacement current does not constitute charge

passing through the dielectric of the capacitor (i.e., the MgO barrier). This discovery offers great potential for the development of robust MTJ devices capable of operating under high current conditions. Additionally, our research underscores the significance of considering capacitive impedance when analyzing high-frequency magnetotransport data.

II. DEVICE FABRICATION AND TMR MEASUREMENTS

Figures 1(a) and 1(b) show an optical image and a cross-section schematic diagram of the MTJ device used in this study, respectively. First, a multilayer of W (5 nm)/CoFeB (1.3 nm)/MgO (2.5 nm)/CoFeB (5 nm)/Ta (5 nm)/Ru (5 nm) was deposited on top of an oxidized Si substrate using magnetron sputtering. Then, using a two-step lithography and etching process, the bottom W/CoFeB/MgO heterostructure was patterned into a microwire, while the following top CoFeB/Ta/Ru layers were patterned into a nanopillar [Fig. 1(b)]. Subsequently, 20-nm SiO_2 was deposited to electrically isolate a 40-nm-thick Pt top electrode from the bottom W/CoFeB electrode. In this study, we used a device with an MTJ diameter of ~1.5 μm and a resistance-area product of the 2.5-nm-thick MgO tunnel barrier of 1 MΩ μm^2.

We then performed DC magnetotransport measurements to determine the variation of the TMR as a function of the in-plane magnetic field (B_y). Figure 1(c) shows the measurements of the MTJ device used in this experiment. In the bottom W/CoFeB/MgO multilayer, the CoFeB thickness is 1.3 nm, for which the total magnetic anisotropy is expected to be a mixture of bulk in-plane and interfacial out-of-plane anisotropy [25]. The bulk in-plane anisotropy component is almost uniform along different
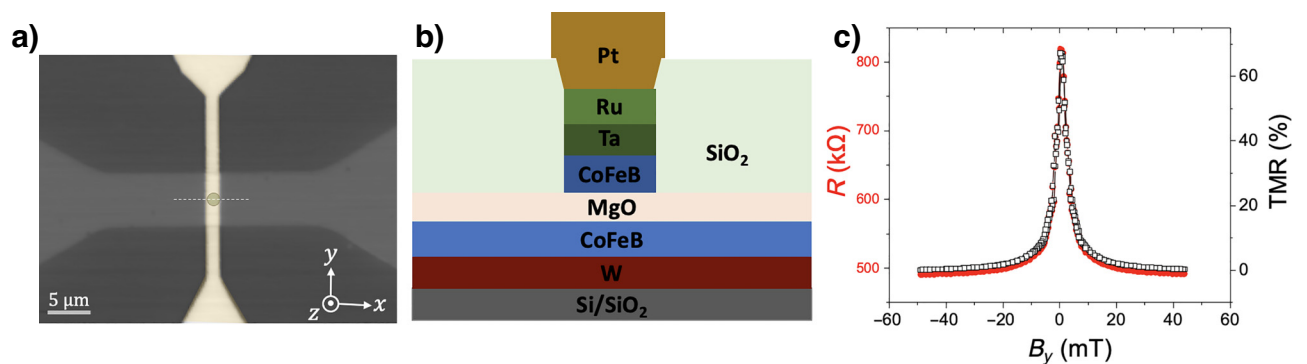

FIG. 1.   (a) Top view (optical micrograph) of the 1.5-μm-diameter device with the Pt top electrode in the center highlighted in yellow and the MTJ pillar in faint green, respectively. The bottom W/CoFeB/MgO microwire is perpendicular to the Pt electrode. (b) Schematic diagram of the cross-section of the layer structure at the device region marked by white dotted line in panel (a). (c) Magnetotransport measurements showing the variation of resistance (red, left-hand axis) and corresponding TMR (black, right-hand axis) as a function of the in-plane magnetic field.

in-plane directions in the x-y plane. The device was then annealed at 400 °C in a high-vacuum furnace to improve both TMR and interfacial out-of-plane anisotropy [26] (see Sec. I of the Supplemental Material [34]). The top CoFeB layer thickness is 5 nm and is, therefore, dominated by bulk in-plane anisotropy. The combination of anisotropies of the bottom and top CoFeB layers leads to the observed TMR curve as a function of B_y shown in Fig. 1(c), where the remanent in-plane magnetization of the top CoFeB layer forms an angle between 0° to 90° with the out-of-plane tilted remanent magnetization of the bottom CoFeB layer, giving a high resistance state. The bottom layer can be easily saturated into a parallel in-plane magnetization direction by applying approximately $>|20|$ mT, producing low resistance states. A TMR ratio of up to 70% was observed between the remanent and saturated magnetic states. The large TMR proves an efficient spin tunneling through MgO, while the variation of the TMR with respect to the magnetic field confirms the remanent magnetization states of the two CoFeB layers and their variation under the applied magnetic field. The net out-of-plane tilted anisotropy of the bottom CoFeB layer is ideal for obtaining magnetization dynamics under voltage and current applications, which is discussed in later sections.

III. STUDY OF MAGNETIZATION DYNAMICS

The magnetization dynamics in the bottom W/CoFeB microwire region were explored under different electrical excitations using time-resolved magneto-optical Kerr effect (TR-MOKE) microscopy. Magnetization dynamics were probed using ultrafast laser pulses derived from a mode-locked fiber laser operating at a wavelength of 1040 nm and a repetition rate of 80 MHz. The laser pulses with a nominal duration of 140 fs were frequency doubled by means of optical second harmonic generation to produce probe pulses with a wavelength of 520 nm. The beam was passed along a quad-pass optical delay line for up to 8 ns of optical time delay with subpicosecond temporal resolution. The beam was expanded ×2 to reduce beam divergence, linearly polarized, and focused to a diffraction-limited spot using a long working distance ×50 (numerical aperture 0.55) microscope objective lens to achieve a spatial resolution of ∼400 nm. The reflected probe laser pulses were collected using the same lens and the change in polarization was detected using a polarizing balanced photodiode bridge detector. Measurements were made in the polar MOKE configuration that allows the out-of-plane component of the dynamic magnetization (ΔM_z) [27] to be detected when the device is magnetized in-plane by an in-plane field generated by a calibrated permanent magnet assembly. The TR-MOKE microscope was used for two types of measurements [20], i.e., to reveal either the temporal or spatial evolution of magnetization dynamics by

fixing either the position or the time delay, respectively. In the first case, the probe laser spot was fixed at a selected position on the bottom electrode, as shown in Fig. 2(a), and the variation in the TR-MOKE signal as a function of time delay was recorded. In the second case, the sample position was scanned beneath the probe laser spot while the time delay remained fixed, allowing the spatial character of magnetization dynamics at a particular time delay to be imaged across the entire bottom electrode.

Magnetization dynamics were excited by applying either an electrical voltage impulse or a microwave voltage waveform to the device. Voltage impulses synchronized to the laser repetition rate at 80 MHz were produced with nominal rise time, duration, and amplitude of 30 ps, 70 ps, and −5 V, respectively. The resulting broadband excitation stimulates the precession of the bottom electrode magnetization at the ferromagnetic resonance (FMR) frequency corresponding to the bias magnetic field applied to the device. To isolate the spatial character of the FMR mode, a microwave comb generator was used to apply a single frequency microwave voltage waveform to the device. A microwave comb containing multiples of 80 MHz from 160 MHz to 18 GHz was generated from an 80 MHz input signal derived from the laser repetition rate. The microwave comb was filtered using narrow pass notch filters with <80 MHz bandwidth to leave just the frequency component corresponding to the FMR. The amplitude of the microwave waveform was adjusted using a combination of microwave amplification and attenuation. For each excitation type, the voltage impulse or waveform was passed through a directional coupler for monitoring using a sampling oscilloscope. A bias tee was used to decouple the impulse and comb generators from the device, which minimized the risk of electrostatic damage to the device when making electrical connections while allowing the TMR to be monitored using the DC port of the bias tee. Finally, the output of the impulse or comb generator was amplitude modulated at ∼31.4 kHz, leading to a modulation of the device excitation and resulting polar Kerr signal, which was then recovered using a lock-in amplifier.

The unique geometry of our device, as illustrated in Figs. 1(b) and 2(a), offers two distinct advantages. Firstly, it enables the application of electrical input either vertically through the MTJ from the top to the bottom electrode, or horizontally through the top or bottom electrodes separately. Secondly, since the bottom CoFeB electrode extends beyond the width of the MTJ and nonmagnetic top contact, it is possible to investigate magnetization dynamics in the vicinity of the MTJ, namely, the propagation of spin waves that may originate from beneath the pillar and propagate along the bottom CoFeB electrode and any steady-state magnetization dynamics in the entire bottom CoFeB region [28]. Considering these possibilities, we investigated magnetization dynamics within the microwire region of the W/CoFeB by applying two types of electrical
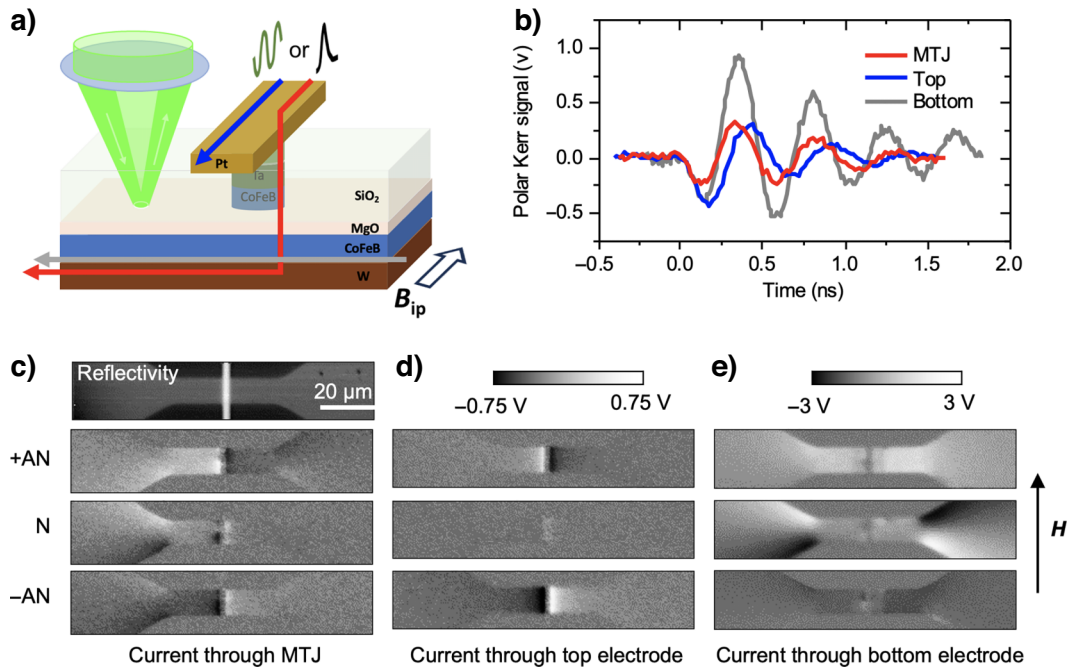
FIG. 2.   (a) Schematic view of the TR-MOKE experiment in which the input is either applied in the form of a voltage pulse (black) or rf wave (green). The red, blue, and gray arrows represent the current paths for the input signals applied through the MTJ, top electrode, and bottom electrode, respectively. For the first case (red), the current path also includes part of the top and bottom electrodes. (b) Plot of the Kerr rotation versus time delay taken after fixing the laser spot at the left-hand side of the top electrode, as shown in Fig. 1(b), and applying an input voltage pulse across the MTJ (red), top electrode (blue), and bottom electrode (gray). Spatially resolved TR-MOKE images taken at a fixed time delay correspond to the first +antinode (+AN), node (N), and −antinode (−AN) of the plot shown in (b), after applying the input voltage across the (c) MTJ, (d) top electrode, and (e) bottom electrode. The optical reflectivity image of the device is shown in the top panel of (c), where the bottom CoFeB microwire electrode (gray with tapered section to the left and right of the center), on which the TR-MOKE scanning was performed, and the position of the top electrode (orthogonal white line at the center) are indicated.

input signals: (i) a voltage impulse with a rise time of 30 ps and a duration of 70 ps and (ii) an rf excitation of fixed frequency (i.e., 2 GHz). The results of each of these cases are separately discussed below.

IV. MAGNETIZATION DYNAMICS UNDER A VOLTAGE PULSE

In the presence of $B_y = 75$ mT, a 70-ps voltage pulse with an amplitude of 930 mV was applied across the MTJ, with the expected current path indicated by the red arrow in Fig. 2(a). Subsequently, we measured the corresponding TR-MOKE variation on the left-hand side of the MTJ, a distance ∼1 μm from the top electrode [Fig. 2(a)]. As shown by the red curve in Fig. 2(b), we observed an oscillating TR-MOKE signal that gradually decayed over time, confirming the detection of magnetization precession. The time required to complete one cycle of precession is ∼0.5 ns, corresponding to a frequency of approximately 2 GHz. Subsequently, we confirmed that this frequency matched the resonance frequency at $B_y = 75$ mT (see Sec. II of the Supplemental Material [34]). This means that

while the broadband voltage pulse can, in principle, induce magnetization precession at random multiple frequencies, only the precessional component at 2 GHz, that is, at resonance for the applied field of $B_y = 75$ mT, contributes to the observed TR-MOKE signal.

To understand the spatial distribution of the magnetization precession, we then conducted TR-MOKE scans of the entire W/CoFeB microwire region, as shown in Fig. 2(c), at three different time delays that correspond to nodes and antinodes of the time-varying signal in Fig. 2(b). Interestingly, we observed a predominant spin precession in the immediate vicinity of the top electrode (vertical strip at the center of the reflectivity image), with opposite ΔM_z on its left-hand and right-hand sides. Any magnetization dynamics beneath the top contact were not observed since the Pt top contact thickness was larger than the optical skin depth, resulting in a narrow vertical strip of negligible signal in the TR-MOKE images.

To identify the mechanism giving rise to the results shown in Fig. 2(c), we first need to consider four different scenarios through which the applied voltage pulse can induce magnetization dynamics, as illustrated in
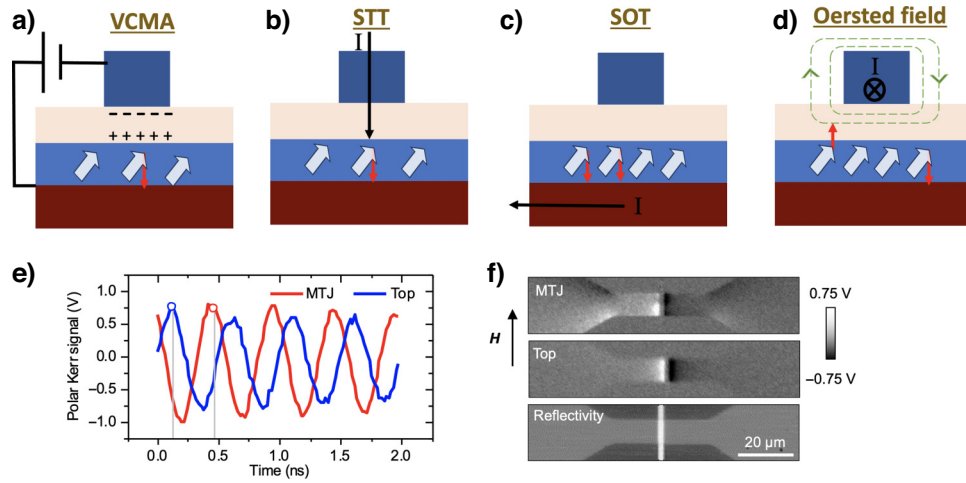
FIG. 3.   Schematic diagram illustrating the possible origins of magnetization dynamics (white arrows) under and on the two sides of the top electrode: (a) VCMA, (b) STT, (c) SOT, and (d) the Oersted field. (e) Polar MOKE signal versus time delay when applying an input voltage of 2 GHz across the MTJ (red) and the top electrode (blue). (f) Corresponding spatial scans for the same input voltage applied across the MTJ (above) and the top electrode (below) taken at a fixed time delay indicated in panel (e).

Figs. 3(a)–3(d): (i) voltage-controlled magnetic anisotropy (VCMA) variation at the CoFeB/MgO interface underneath the pillar region, launching propagating spin waves [29]; (ii) spin-transfer torque (STT) in the pillar region inducing propagating spin waves [30]; (iii) spin-orbit torque (SOT) inducing magnetization precession in the entire W/CoFeB microwire region [31] (see Sec. IV of the Supplemental Material [34] for details); and (iv) an Oersted field from the top electrode inducing spin precession in the W/CoFeB microwire region. We have performed micromagnetic simulations (shown in the Supplemental Material [34], Sec. VIII) to further verify the expected magnetization dynamics depicted in Figs. 3(a)–3(d). Among the above four possibilities, we can conclusively determine that the observation in Fig. 2(c) is related to case (iv). For cases (i) and (ii), we would see spin wave propagation toward both sides of the top electrode with the same sign for ΔM_z. For case (iii), we should observe steady-state spin precession with the same sign of ΔM_z along the entire W/CoFeB microwire region in which the current flows (from the left-hand side to the top electrode). Thus, the only effect that can result in spin precession with opposite ΔM_z on the two sides of the top electrode, as observed in Fig. 3(a), is related to case (iv). This is because the Oersted field induced by the current on the left-hand and right-hand sides of the top electrode is pointing in opposite directions. However, to generate a large enough Oersted field to create such magnetization dynamics, a high current of the order of mA is typically required (see Sec. III of the Supplemental Material [34]). Considering that the MTJ resistance is ∼490 kΩ for $B_y > 20$ mT, as determined in the DC-TMR measurement [Fig. 1(c)], the maximum current expected from a voltage pulse of 930 mV is ∼1.86 μA.

This current is too small to generate a strong enough Oersted field, suggesting that a much larger current must flow through the top electrode when applying a high-frequency pulse.

To verify the above scenario, we repeated the same TR-MOKE measurement protocol with the voltage pulse being applied solely through the top electrode [indicated by the blue arrow in Fig. 2(a)], which has a resistance of ∼110 Ω. We then adjusted the amplitude of this voltage pulse to ∼375 mV to achieve a similar TR-MOKE signal amplitude to that observed when applying 930 mV across the MTJ, as shown in Fig. 2(b). This corresponds to a current flow of ∼3.5 mA, which unambiguously confirms that when applying a 930-mV pulse across the MTJ, the actual current flowing through the top electrode is more than three orders of magnitude larger than the expected current extracted from DC measurements (1.86 μA), indicating the presence of a frequency-dependent impedance effect in our MTJ circuit.

When a voltage pulse is applied across the MTJ, the current also flows through both the top and bottom electrodes, as indicated by the red arrow in Fig. 2(a). In addition to the TR-MOKE contrast observed due to the Oersted field-induced magnetization dynamics near the top electrode, TR-MOKE contrast was also observed in the bottom electrode (W/CoFeB) region, as shown in Fig. 2(c). The MOKE contrast is more pronounced on the left-hand side of the top electrode, where a large current flows. The bottom electrode consists of three regions: a straight wire region in the middle where the current is expected to flow along the x-axis, and two triangular-shaped regions on either side where the current flow has both x and y components. Two important features were observed in the

TR-MOKE images shown in Fig. 2(c): (i) a large contrast where the current diverges from the middle straight wire region to the triangular regions and (ii) opposite contrasts along the two diagonals of the triangular region. Both features can be indistinguishably attributed to either the Oersted field or SOT-induced magnetization dynamics (for details, see Secs. IV and VIII of the Supplemental Material [34]). If an Oersted field is generated due to current flowing through the bottom electrode, its y-component acts on the magnetization in the middle wire region, while both the x and y components act on magnetization in the triangular region. However, since magnetization is fixed along the y-axis by the external applied field, only the x-component of the Oersted field creates magnetization dynamics along the z-axis, resulting in the observed MOKE contrast being larger in the triangular region. The x-component of the Oersted field is opposite along the two diagonals in the same triangular region, resulting in the observed opposite contrasts. Interestingly, the action of damping-like SOT creates an effective out-of-plane field and, thus, magnetization dynamics along $+z$ and $-z$ directions have the same symmetry as the Oersted field-induced magnetization dynamics (for details, see Sec. IV of the Supplemental Material [34]). Therefore, it is not possible to distinguish between the two effects. However, as for the case of the top electrode explained earlier, only a current on the order of mA generates the large Oersted field required for magnetization dynamics. Similarly, SOT-induced magnetization dynamics in W/CoFeB usually require a large current density on the order of at least 10^{10} A/m^2 [32] and, considering the dimensions of our device, a current on the order of mA will be required. This further confirms a large current flow of the order of mA in our MTJ circuits.

To further confirm the origin of the magnetization dynamics of the bottom electrode, we repeated the TR-MOKE experiment by applying a voltage pulse (corresponds to a current of ~1 mA) only across the bottom electrode [indicated by the gray arrow in Fig. 2(a)], the resulting TR-MOKE image is shown in Fig. 2(e). Again, a large TR-MOKE contrast was observed in a triangular region, as well as opposite contrasts along the two diagonals of the triangular region. This further confirms the action of either the Oersted field and/or SOT-induced magnetization dynamics in the bottom electrode (see Sec. IV of the Supplemental Material [34]).

V. MAGNETIZATION DYNAMICS FOR RF WAVE INPUT

As shown above, the application of a 70-ps voltage pulse initiates magnetization dynamics at the resonance frequency of 2 GHz. However, given that a voltage pulse should excite a broad band of frequencies, it is possible that only a fraction of the voltage amplitude (930 mV across the MTJ and 375 mV across the top electrode) contributes

to the magnetization dynamics at 2 GHz, resulting in a smaller TR-MOKE signal (per input voltage). To validate the full effect of the amplitude of the high-frequency input signal, we conducted the same experiments as shown in Fig. 2, but this time using a sine wave input signal at 2 GHz [indicated by the green wave in Fig. 2(a)]. As expected, the magneto-optical signal:input voltage ratio is larger in this case [Fig. 3(e)]. A continuously oscillating TR-MOKE signal without decay was obtained, confirming the one-to-one correlation between the continuous precession of magnetization and the continuous input wave signal. Importantly, similar to the observation in Fig. 2, the TR-MOKE spatial scan [Fig. 3(f)] displays opposite precession signals near the two sides of the top electrode, confirming the Oersted field-induced magnetization dynamics. The amplitudes of the TR-MOKE signals, when applying the input wave with a peak-to-peak voltage (V_{p-p}) of ~550 mV across the MTJ (corresponding to $I \approx 1.1$ μA) and 250 mV across the top electrode (corresponding to $I \approx 2.2$ mA), were almost the same, as shown by the red and blue curves in Fig. 3(e), respectively. This again confirms that, at high frequencies, the total impedance in our circuit is more than three orders of magnitude lower than in the DC resistance case.

VI. DISCUSSION

To elucidate our findings, it is necessary to examine an MTJ circuit model in which the overall impedance diminishes as the frequency increases. One plausible approach involves accounting for the capacitance effect of the MTJ. In this context, we can regard the MTJ as a parallel resistance-capacitance (RC) circuit, with MgO functioning as the dielectric of the capacitor. An expression for the overall magnitude of the impedance of the MTJ is given as follows:

$$Z = \frac{1}{\sqrt{(1/R)^2 + (2\pi f C)^2}},$$

where f and C are frequency and capacitance, respectively. For a parallel plate capacitor with one plate having an infinite area, the geometrical capacitance (C) can be written as follows (for details, see Sec. V of the Supplemental Material [34]):

$$C = \frac{2\varepsilon_0 \varepsilon_r A}{d},$$

where A and d are the area of MTJ pillar and MgO thickness, respectively. Thus, Z depends on the frequency and area that is proportional to the square of the radius of the device, which is ~750 nm for our MTJ. For $V = 930$ mV, we calculated the overall current flow at different frequencies ($I = V/Z$), as shown in Fig. 4 for different MTJ sizes with the green curve representing our MTJ. We clearly see that in the GHz regime (indicated by the gray area in Fig. 4), the current flow in the circuit is on the order of a few mA instead of the μA range expected from the
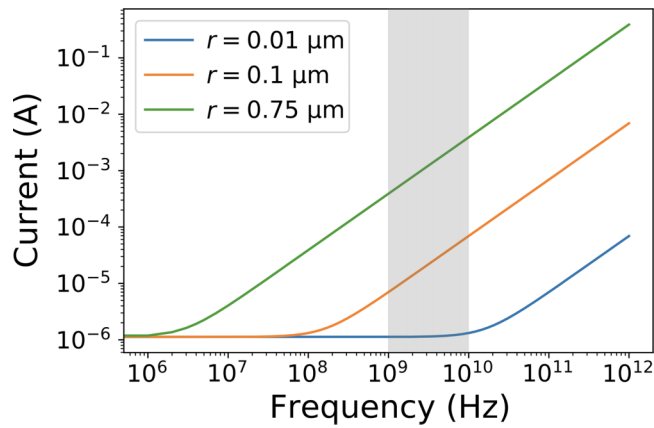
FIG. 4. Plot of current versus frequency for an MTJ modeled as a parallel RC circuit.

DC measurements. In our device, the substrate Si/SiO_2 can also act as a capacitor, allowing displacement current across them in parallel to the MTJ circuit, depending on the resistivity of Si. This may influence the total displacement current in the MTJ circuit, as explained in the Supplemental Material, Sec. IX [34].

The current flowing through the capacitor at high frequencies, i.e., the displacement current, does not involve the actual flow of charges through the dielectric barrier. The RC time constant defines the charging and discharging of the capacitor (see Sec. VI of the Supplemental Material [34]), which is ~55 ns for our device. This time constant is significantly larger than the period of the input wave, which is 0.5 ns at 2 GHz. At such a short timescale, the accumulation of charge responsible for the resistance in the capacitor (MgO) is expected to be extremely low. This, in turn, permits a significant displacement current flow in the outer circuit of the MTJ capacitor; the top and bottom electrodes are included in this outer circuit. It is this large displacement current that gives rise to the observed magnetization dynamics attributed to the induced Oersted field and SOT effects.

Our findings will be applicable to various MTJ-related applications and rf measurement schemes. The large displacement current we have observed holds significant potential for inducing magnetization dynamics for device applications, such as SOT-induced magnetization switching and the propagation of Oersted-field-driven spin waves. Notably, this displacement does not cause a charge current to flow across the MgO barrier, thus posing only a low risk for barrier breakdown in MTJ devices. However, while these advantages are evident, the displacement current may not be desirable in certain applications, such as high-frequency TMR reading. To address this concern, reducing the capacitance effect can be achieved by shrinking the size of the MTJ pillar (i.e., the area of the parallel plate capacitor). To explore this relationship, we conducted calculations to determine the net current flow for MTJs with radii of 100 and 10 nm under the same voltage conditions as those used in our experiments, as depicted in Fig. 4. For sub-100-nm MTJs, the displacement current in the mA range is expected to be beyond the 100 GHz range.

Finally, our finding also impacts rf techniques such as spin torque [18] or voltage-FMR [33], which are often measured at GHz frequencies, where MTJs of a similar size to those in our experiments are commonly employed. Here, the current flow is usually calculated by assuming MgO as a resistive barrier. However, we conclude that it is important to reevaluate this assumption by considering the MTJ as an RC circuit, where the current flow can be significantly higher. Given that this displacement current does not pass through the MgO barrier, STT might not be present, while the influence of SOT or the Oersted field becomes a defining factor in magnetization dynamics, as unequivocally demonstrated in our experiments.

ACKNOWLEDGMENT

[1] S. Bhatti, R. Sbiaa, A. Hirohata, H. Ohno, S. Fukami, and S. N. Piramanayagam, Spintronics based random access memory: A review, Mater. Today **20**, 530 (2017).

[2] S. S. P. Parkin, C. Kaiser, A. Panchula, P. M. Rice, B. Hughes, M. Samant, and S. H. Yang, Giant tunnelling magnetoresistance at room temperature with MgO (100) tunnel barriers, Nat. Mater. **3**, 862 (2004).

[3] S. Yuasa, T. Nagahama, A. Fukushima, Y. Suzuki, and K. Ando, Giant room-temperature magnetoresistance in single-crystal Fe/MgO/Fe magnetic tunnel junctions, Nat. Mater. **3**, 868 (2004).

[4] D. D. Djayaprawira, K. Tsunekawa, M. Nagai, H. Maehara, S. Yamagata, N. Watanabe, S. Yuasa, Y. Suzuki, and K. Ando, 230% room-temperature magnetoresistance in CoFeBMgOCoFeB magnetic tunnel junctions, Appl. Phys. Lett. **86**, 092502 (2005).

[5] E. E. Fullerton and J. R. Childress, Spintronics, magnetoresistive heads, and the emergence of the digital world, Proc. IEEE **104**, 1787 (2016).

[6] R. C. Sousa and I. L. Prejbeanu, Non-volatile magnetic random access memories (MRAM), C. R. Phys. **6**, 1013 (2005).

[7] D. C. Ralph and M. D. Stiles, Spin transfer torques, J. Magn. Magn. Mater. **320**, 1190 (2008).

[8] Y. Shiota, T. Nozaki, F. Bonell, S. Murakami, T. Shinjo, and Y. Suzuki, Induction of coherent magnetization switching in a few atomic layers of FeCo using voltage pulses, Nat. Mater. **11**, 39 (2012).

[9] S. I. Klselev, J. C. Sankey, I. N. Krivorotov, N. C. Emley, R. J. Schoelkopf, R. A. Buhrman, and D. C. Ralph, Microwave oscillations of a nanomagnet driven by a spin-polarized current, Nature **425**, 380 (2003).

[10] V. E. Demidov, S. Urazhdin, H. Ulrichs, V. Tiberkevich, A. Slavin, D. Baither, G. Schmitz, and S. O. Demokritov, Magnetic nano-oscillator driven by pure spin current, Nat. Mater. **11**, 1028 (2012).

[11] A. M. Deac, A. Fukushima, H. Kubota, H. Maehara, Y. Suzuki, S. Yuasa, Y. Nagamine, K. Tsunekawa, D. D. Djayaprawira, and N. Watanabe, Bias-driven high-power microwave emission from MgO-based tunnel magnetoresistance devices, Nat. Phys. **4**, 803 (2008).

[12] Y. Shiota, S. Murakami, F. Bonell, T. Nozaki, T. Shinjo, and Y. Suzuki, Quantitative evaluation of voltage-induced magnetic anisotropy change by magnetoresistance measurement, Appl. Phys. Express **4**, 043005 (2011).

[13] M. Harder, Y. Gui, and C. M. Hu, Electrical detection of magnetization dynamics via spin rectification effects, Phys. Rep. **661**, 1 (2016).

[14] A. A. Tulapurkar, Y. Suzuki, A. Fukushima, H. Kubota, H. Maehara, K. Tsunekawa, D. D. Djayaprawira, N. Watanabe, and S. Yuasa, Spin-torque diode effect in magnetic tunnel junctions, Nature **438**, 339 (2005).

[15] A. V. Chumak, *et al.*, Advances in magnetics roadmap on spin-wave computing, IEEE Trans. Magn. **58**, 0800172 (2022).

[16] R. Sharma, R. Mishra, T. Ngo, Y. X. Guo, S. Fukami, H. Sato, H. Ohno, and H. Yang, Electrically connected spin-torque oscillators array for 2.4 GHz WiFi band transmission and energy harvesting, Nat. Commun. **12**, 2924 (2021).

[17] J. Torrejon, Mathieu Riou, Flavio Abreu Araujo, Sumito Tsunegi, Guru Khalsa, Damien Querlioz, Paolo Bortolotti, Vincent Cros, Kay Yakushiji, Akio Fukushima, Hitoshi Kubota, Shinji Yuasa, Mark D. Stiles, and Julie Grollier, Neuromorphic computing with nanoscale spintronic oscillators, Nature **547**, 428 (2017).

[18] J. C. Sankey, Y. T. Cui, J. Z. Sun, J. C. Slonczewski, R. A. Buhrman, and D. C. Ralph, Measurement of the spin-transfer-torque vector in magnetic tunnel junctions, Nat. Phys. **4**, 67 (2008).

[19] H. Kubota, Akio Fukushima, Kay Yakushiji, Taro Nagahama, Shinji Yuasa, Koji Ando, Hiroki Maehara, Yoshinori Nagamine, Koji Tsunekawa, David D. Djayaprawira, Naoki Watanabe, and Yoshishige Suzuki, Quantitative measurement of voltage dependence of spin-transfer torque in MgO-based magnetic tunnel junctions, Nat. Phys. **4**, 37 (2008).

[20] H. Kaiju, S. Fujita, T. Morozumi, and K. Shiiki, Magnetocapacitance effect of spin tunneling junctions, J. Appl. Phys. **91**, 7430 (2002).

[21] G. Landry, Y. Dong, J. Du, X. Xiang, and J. Q. Xiao, Interfacial capacitance effects in magnetic tunneling junctions, Appl. Phys. Lett. **78**, 501 (2001).

[22] P. Padhan, P. Leclair, A. Gupta, K. Tsunekawa, and D. D. Djayaprawira, Frequency-dependent magnetoresistance and magnetocapacitance properties of magnetic tunnel junctions with MgO tunnel barrier, Appl. Phys. Lett. **90**, 142105 (2007).

[23] S. Parui, M. Ribeiro, A. Atxabal, A. Bedoya-Pinto, X. Sun, R. Llopis, F. Casanova, and L. E. Hueso, Frequency driven inversion of tunnel magnetoimpedance and observation of positive tunnel magnetocapacitance in magnetic tunnel junctions, Appl. Phys. Lett. **109**, 052401 (2016).

[24] T. Nakagawa, K. Ogata, Y. Nakayama, G. Xiao, and H. Kaiju, Sign inversion phenomenon of voltage-induced tunnel magnetocapacitance, Appl. Phys. Lett. **118**, 182403 (2021).

[25] S. Ikeda, K. Miura, H. Yamamoto, K. Mizunuma, H. D. Gan, M. Endo, S. Kanai, J. Hayakawa, F. Matsukura, and H. Ohno, A perpendicular-anisotropy CoFeB-MgO magnetic tunnel junction, Nat. Mater. **9**, 721 (2010).

[26] W. Skowroński, T. Nozaki, D. D. Lam, Y. Shiota, K. Yakushiji, H. Kubota, A. Fukushima, S. Yuasa, and Y. Suzuki, Underlayer material influence on electric-field controlled perpendicular magnetic anisotropy in CoFeB/MgO magnetic tunnel junctions, Phys. Rev. B **91**, 184410 (2015).

[27] A. Barman, T. Kimura, Y. Otani, Y. Fukuma, K. Akahane, and S. Meguro, Benchtop time-resolved magneto-optical Kerr magnetometer, Rev. Sci. Instrum. **79**, 123905 (2008).

[28] P. S. Keatley, S. R. Sani, G. Hrkac, S. M. Mohseni, P. Dürrenfeld, T. H. J. Loughran, J. Åkerman, and R. J. Hicken, Direct observation of magnetization dynamics generated by nanocontact spin-torque vortex oscillators, Phys. Rev. B **94**, 060402 (2016).

[29] B. Rana, Y. Fukuma, K. Miura, H. Takahashi, and Y. Otani, Excitation of coherent propagating spin waves in ultra-thin CoFeB film by voltage-controlled magnetic anisotropy, Appl. Phys. Lett. **111**, 52404 (2017).

[30] M. Madami, S. Bonetti, G. Consolo, S. Tacchi, G. Carlotti, G. Gubbiotti, F. B. Mancoff, M. A. Yar, and J. Åkerman, Direct observation of a propagating spin wave induced by spin-transfer torque, Nat. Nanotechnol. **6**, 635 (2011).

[31] C. Kim, Byong Sun Chun, Jungbum Yoon, Dongseuk Kim, Yong Jin Kim, In Ho Cha, Gyu Won Kim, Dae Hyun Kim, Kyoung-Woong Moon, Young Keun Kim, and Chanyong Hwang, Spin-orbit torque driven magnetization switching and precession by manipulating thickness of CoFeB/W heterostructures, Adv. Electron. Mater. **6**, 1901004 (2020).

[32] C. F. Pai, L. Liu, Y. Li, H. W. Tseng, D. C. Ralph, and R. A. Buhrman, Spin transfer torque devices utilizing the giant spin Hall effect of tungsten, Appl. Phys. Lett. **101**, 122404 (2012).

[33] T. Nozaki, Yoichi Shiota, Shinji Miwa, Shinichi Murakami, Frédéric Bonell, Shota Ishibashi, Hitoshi Kubota, Kay Yakushiji, Takeshi Saruya, Akio Fukushima, Shinji Yuasa,

Teruya Shinjo, and Yoshishige Suzuki, Electric-field-induced ferromagnetic resonance excitation in an ultra-thin ferromagnetic metal layer, Nat. Phys. **8,** 491 (2012).

[34] See Supplemental Material at http://link.aps.org/supplemental/10.1103/PhysRevApplied.22.024019 which consists of TMR study as a function of MTJ annealing conditions, TR-MOKE measurement of the ferromagnetic resonance, calculation of the Oersted field due to a top electrode current, discussion about SOT and Oersted field induced magnetization dynamics in the bottom electrode, derivation of equation to determine capacitance of a parallel plate capacitor of varying area, Calculation of charging and discharging of the MTJ capacitor, TR-MOKE measurements to confirm the reproducibility of our results, Micromagnetic simulations, and a discussion about substrate RF current effects. The supplemental material also contains Refs. [35–38].

[35] W. Skowroński, T. Nozaki, D. D. Lam, Y. Shiota, K. Yakushiji, H. Kubota, A. Fukushima, S. Yuasa, and Y. Suzuki, Underlayer material influence on electric-field controlled perpendicular magnetic anisotropy in CoFeB/MgO magnetic tunnel junctions, Phys. Rev. B **91,** 184410 (2015).

[36] A. Vansteenkiste, J. Leliaert, M. Dvornik, M. Helsen, F. Garcia-Sanchez, and B. Van Waeyenberge, The design and verification of MuMax3, AIP Adv. **4,** 107133 (2014).

[37] M. Abbasi, B. Wang, S. Tamaru, H. Kubota, A. Fukushima, and D. S. Ricketts, Accurate de-embedding and measurement of spin-torque oscillators, IEEE. Trans. Magn. **53,** 1400904 (2017).

[38] D. Jiang, H. Chen, G. Ji, Y. Chai, C. Zhang, Y. Liang, J. Liu, W. Skowronski, P. Yu, D. Yi, and T. Nan, Substrate-induced spin-torque-like signal in spin-torque ferromagnetic resonance measurement, Phys. Rev. Appl. **21,** 024021 (2024).